⁶Long-Term Evaluation of Temperature Profiles Measured by an Operational Raman Lidar

ROB K. NEWSOM

Pacific Northwest National Laboratory, Richland, Washington

DAVID D. TURNER

NOAA/National Severe Storms Laboratory, Norman, Oklahoma

JOHN E. M. GOLDSMITH

Sandia National Laboratories, Livermore, California

(Manuscript received 2 July 2012, in final form 7 November 2012)

ABSTRACT

This study investigates the accuracy and calibration stability of temperature profiles derived from an operational Raman lidar over a 2-yr period from 1 January 2009 to 31 December 2010. The lidar, which uses the rotational Raman technique for temperature measurement, is located at the U.S. Department of Energy's Atmospheric Radiation Measurement site near Billings, Oklahoma. The lidar performance specifications, data processing algorithms, and the results of several test runs are described. Calibration and overlap correction of the lidar is achieved using simultaneous and collocated radiosonde measurements. Results show that the calibration coefficients exhibit no significant long-term or seasonal variation but do show a distinct diurnal variation. When the diurnal variation in the calibration is not resolved the lidar temperature bias exhibits a significant diurnal variation. Test runs in which only nighttime radiosonde measurements are used for calibration show that the lidar exhibits a daytime warm bias that is correlated with the strength of the solar background signal. This bias, which reaches a maximum of ~2.4 K near solar noon, is reduced through the application of a correction scheme in which the calibration coefficients are parameterized in terms of the solar background signal. Comparison between the corrected lidar temperatures and the noncalibration radiosonde temperatures show a negligibly small median bias of -0.013 K for altitudes below 10 km AGL. The corresponding root-mean-square difference profile is roughly constant at ~2 K below 6 km AGL and increases to about 4.5 K at 10 km AGL.

1. Introduction

Routine measurements of temperature profiles through the depth of the troposphere are crucial for numerical weather prediction, investigating many atmospheric processes, and long-term climate monitoring. Radiosondes continue to be the de facto standard for such measurements. Although these instruments generally provide accurate measurements of temperature and other

3Denotes Open Access content.

Corresponding author address: Rob K. Newsom, Pacific Northwest National Laboratory, 902 Battelle Blvd., P.O. Box 999, MSIN K9-30, Richland, WA 99352.

E-mail: rob.newsom@pnnl.gov

DOI: 10.1175/JTECH-D-12-00138.1

variables, their operation can be expensive and labor intensive. Thus, most operational sites around the world only launch radiosondes on a twice-daily basis, resulting in temporally undersampled observations, particularly in the lower troposphere. Remote sensing techniques offer the potential for autonomous operation and improved temporal resolution, but the uncertainties need to be carefully quantified by comparison against current standards (i.e., radiosonde observations). Such comparisons should be performed over long periods of time (i.e., years) in order to develop a large statistical sample size and to detect any diurnal and/or seasonal variations in accuracy.

A number of atmospheric temperature remote sensing techniques have been demonstrated and implemented operationally over the years. These include active techniques such as radio acoustic sounding (Alexander and

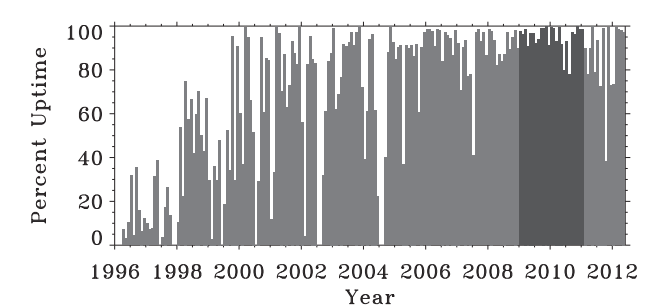


FIG. 1. Monthly average percentage of time that the SGPRL was operational (up time) between 1996 and June 2012. The darker gray indicates the analysis period used in the current study (2009 and 2010). The mean up time between the beginning of 2005 and June 2012 was 90%. The mean up time for 2009 and 2010 was 95%.

Tsuda 2008; Chandrasekhar Sarma et al. 2008), Rayleigh lidar (Li et al. 2011; Alpers et al. 2004), and rotational Raman (RR) lidar, as well as passive techniques that use spectrally resolved microwave or infrared radiometric measurements in combination with statistical or physical retrieval algorithms (Feltz et al. 2003; Loehnert et al. 2009).

Among the lidar techniques, the RR technique is best suited for tropospheric temperature measurement. In the troposphere, inelastic backscatter resulting from rotational transitions in air molecules is strong enough to estimate temperature by measuring changes in the shape of the RR spectrum. In practice, the backscattered energy in two bands of the RR spectrum is measured and temperature is estimated from a ratio of the signals. This measurement technique was first proposed by Cooney (1972) and later demonstrated by Arshinov et al. (1983) using a double-grating monochrometer to achieve narrowband detection of the RR energy at 535 nm. Since that time, other systems based on the RR technique have been developed and demonstrated (Balin et al. 2004; Behrendt and Reichardt 2000; Behrendt et al. 2002, 2004; Di Girolamo et al. 2004; Mattis et al. 2008; Nedeljkovic et al. 1993; Radlach et al. 2008).

In this study, we investigate the accuracy and calibration stability of temperature profiles derived from an operational Raman lidar using the RR technique. The lidar is located at the U.S. Department of Energy's (DOE) Atmospheric Radiation Measurement (ARM) Southern Great Plains (SGP) site near Billings, Oklahoma (36.609°N, 97.487°W). The temperature profiling capability of the SGP Raman lidar (SGPRL) is enabled using interference filters (IFs) to achieve narrowband detection at 355 nm (Di Girolamo et al. 2004).

The SGPRL has been in nearly continuous operation at the SGP central facility since 1996; however, the temperature profiling capability was not added until 2005. Figure 1 shows the monthly percent of time that this

system has been operational since it was initially deployed. The primary role of the SGPRL system is to provide continuous height- and time-resolved measurements of water vapor mixing ratio, temperature, and aerosol and cloud optical properties (Goldsmith et al. 1998; Ferrare et al. 2006; Turner and Goldsmith 1999; Turner et al. 2002). In addition to the Raman lidar, the SGP site contains an extensive suite of instrumentation dedicated to long-term climate observations (Stokes and Schwartz 1994).

The accuracy and calibration stability of the lidar temperature measurements are assessed by comparison with radiosonde data over a 2-yr period from 1 January 2009 to 31 December 2010, as indicated by the dark shaded region in Fig. 1. Radiosondes are launched four times daily at the SGP central facility. This compares to most operational centers where radiosondes are only launched on a twice-daily basis. The radiosonde launch times at SGP nominally occur at 0530, 1130, 1730, and 2330 UTC. The 0530 and 1730 UTC soundings occur during nighttime and near solar noon, respectively, while the 1130 and 2330 UTC soundings occur near dawn and dusk, respectively. This launch schedule provides sufficient temporal resolution to evaluate any diurnal dependence of the accuracy and/or calibration of the lidar-derived temperature profiles. Additionally, the radiosonde launch site and the lidar are essentially collocated, so that both systems sample nearly the same column of air.

The algorithm used to process the RR signals and produce temperature profiles uses radiosonde data to determine calibration coefficients and overlap corrections. In this study, the long-term, seasonal, and diurnal variations in the calibrations are analyzed by configuring the algorithm to use all of the available daily radiosonde profiles. Separate tests are then conducted by configuring the algorithm to use only one radiosonde profile per day for calibration and overlap correction. Biases and root-mean-square (RMS) errors in the lidar temperature data are determined by comparison with those radiosonde profiles that are not used for calibration and overlap correction. This provides a means of assessing diurnal variations in the lidar temperature error due to unresolved variations in the calibration.

The Raman lidar (RL) temperature algorithm was designed to run autonomously, with little or no user intervention. The development effort has involved multiple iterations of the code, and numerous tests were performed by running the code over several years of input data. The work described here is part of a rigorous process to assess the accuracy of the output. The intent is to run the algorithm operationally within the ARM Data Management Facility (DMF) and to make the output available to the general user community through

TABLE 1. Technical specifications of the SGPRL transmitter and the RR receiver channels.

Transmitter						
Laser	Continuum model 9030, frequency-tripled Nd:YAG					
Wavelength	355 nm					
Pulse energy	~300 mJ					
Pulse width	\sim 5 ns					
Pulse repetition frequency	30 Hz					
Receiver						
FOV (wide)	2 mrad	2 mrad				
FOV (narrow)	0.3 mrad	0.3 mrad				
PMTs	Electron tube 9954B					
Data acquisition	Licel transient data recorders with simultaneous analog and photon counting					
Pulse accumulation time	10 s					
Range resolution	7.5 m					
RR IF specifications	RR1 (Low-J)	RR2 (High-J)				
CWL	354.27 nm	353.27 nm				
FWHM	0.22 nm	0.2 nm				
Peak transmission	34%	37%				
Blocking @ 354.7 nm	10^{-7} 10^{-7}					

the ARM website (http://www.arm.gov/). Thus, one goal of this paper is to document the calibration and overlap correction procedures and the quality assurance tests that are used in the algorithm.

This paper is organized as follows. Section 2 provides a brief overview of the ARM Raman lidar at the SGP site. The design and operation of this system have

previously been reported (Goldsmith et al. 1998; Ferrare et al. 2006; Newsom et al. 2009; Turner and Goldsmith 1999; Turner et al. 2002), so the emphasis in section 2 is on those aspects of the system relevant to the temperature measurement. Section 3 describes the processing of the RR signals and the operational temperature algorithm, including the calibration and overlap correction procedures. Section 4 describes the results of several tests that were conducted to determine the calibration stability and accuracy of the lidar-derived temperatures. Finally, a summary is provided in section 5.

2. Raman lidar

The basic design of the SGPRL is described by Goldsmith et al. (1998). Over the years, the system has undergone a number of upgrades, modifications, and additions. In this section, we focus primarily on those aspects of the system relevant to the temperature measurement.

Table 1 provides a summary of the technical specifications of the SGPRL relevant to temperature measurement. The system, which is housed inside an environmentally controlled shipping container, utilizes a frequency-tripled neodymium YAG laser that transmits 300-mJ and 5-ns pulses at a wavelength of 355 nm and a pulse repetition frequency of 30 Hz. The receiver utilizes all free space-coupled optics and contains a total of 10 detection channels, as shown in Fig. 2. Temperature measurements are enabled by the two RR channels labeled RR1 and RR2, which were added to the system in 2005. A boresight

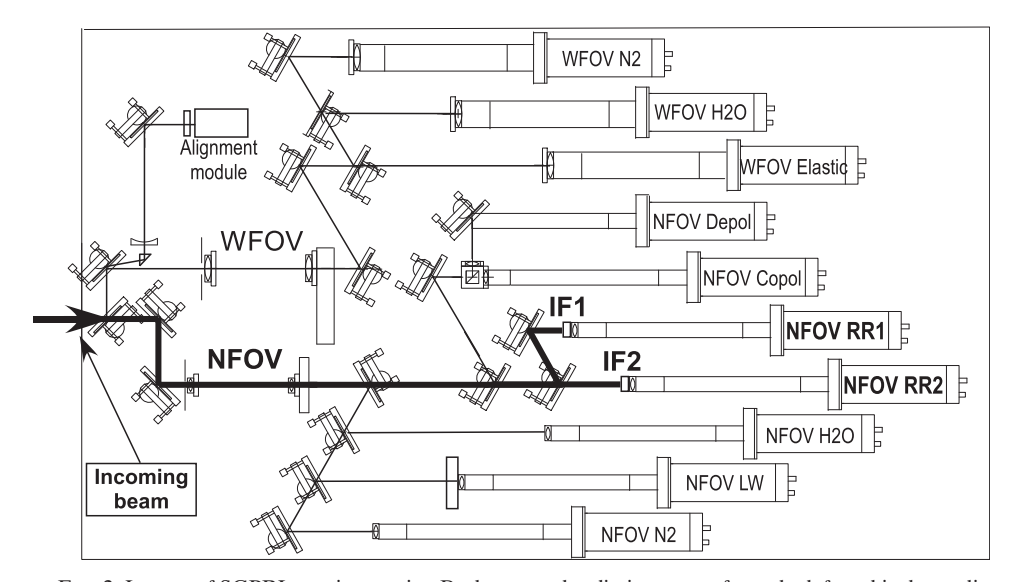


FIG. 2. Layout of SGPRL receiver optics. Backscattered radiation enters from the left and is then split between narrow-field-of-view (NFOV) and wide-field-of-view (WFOV) branches. Both FOVs contain channels for detection of elastically scattered radiation at 355 nm and inelastically (Raman) scattered radiation from atmospheric N₂ at 387 nm and water vapor at 408 nm. The two RR channels (RR1 and RR2) are located only in the NFOV branch. The IFs for RR1 and RR2 are labeled IF1 and IF2, respectively.

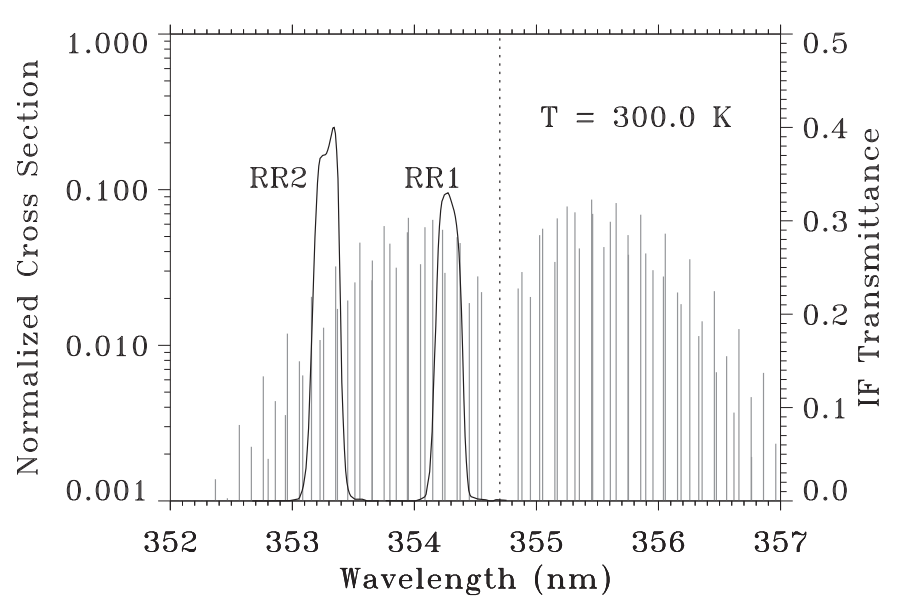


Fig. 3. The RR channel IF transmittances (solid dark) and normalized intensities of the RR lines for air at $300\,\mathrm{K}$ (solid gray). The transmit wavelength is indicated by the vertical dotted line.

alignment module was also added to the system in 2007. The alignment module monitors the position of the laser spot in the receiver's field of view and uses that information to continually adjust the steering of the outgoing beam in order to maintain optimal alignment with the receiver telescope. Preliminary analysis indicates that this feature has improved the alignment stability of the system.

The RR channels sense Raman-shifted backscatter arising from the rotational energy state transitions in atmospheric N_2 and O_2 molecules due to excitation at the laser wavelength of 354.7 nm. These channels use very narrow bandwidth interference filters to measure the energy content in two different portions of the rotational energy spectrum, as illustrated in Fig. 3. The measurements correspond to low- and high-J state transitions, where J denotes the rotational quantum number of the molecule. In the SGPRL, both RR channels measure radiation in the anti-Stokes branch of the rotational spectrum, thereby minimizing the possible influence of fluorescence.

The IFs chosen for such measurement must have a sufficiently high rejection at the laser wavelength to eliminate most of the contribution of the Rayleigh and nearly all of the aerosol backscattered signal. The current design of the SGPRL uses interference filters manufactured by Barr Associates, Inc. The filter in the RR1 (low-J) channel has a center wavelength (CWL) of 354.27 nm and a full width at half maximum (FWHM) of 0.2 nm. The RR2 (high-J) channel incorporates a filter

with a CWL of 353.27 nm and a FWHM of 0.2 nm. The blocking of the laser wavelength is $\sim 10^{-7}$ for both filters, ensuring good isolation of the RR measurements from the aerosol scattering component. This was confirmed operationally, as no cloud-induced backscatter is seen in the RR channels even in low-altitude liquid water cloud situations, where the elastic backscattering by the cloud is large. We estimate the total transmission through the receiver chain (due to losses from the telescope, mirrors, beamsplitters, lenses, and IF) to be about 5%.

The ratio of the RR signals is largely dependent on the temperature of the scattering volume and the effect of incomplete overlap between the outgoing beam and the field of view of the receiver. Differential transmission effects are negligible because the wavelength difference between the two RR channels is small. The height dependence of the ratio of the RR signals (Q) is well approximated by Behrendt and Reichardt (2000):

$$Q(z) = \frac{S_1(z)}{S_2(z)} = O(z) \exp[a + b/T'(z)], \qquad (1)$$

where S_1 and S_2 are the background-subtracted RR signals at 354.3 and 353.3 nm, respectively, O is the overlap function, z is the height above the lidar, a and b are calibration coefficients, and T' is the normalized temperature. For this study, the temperature is normalized according to

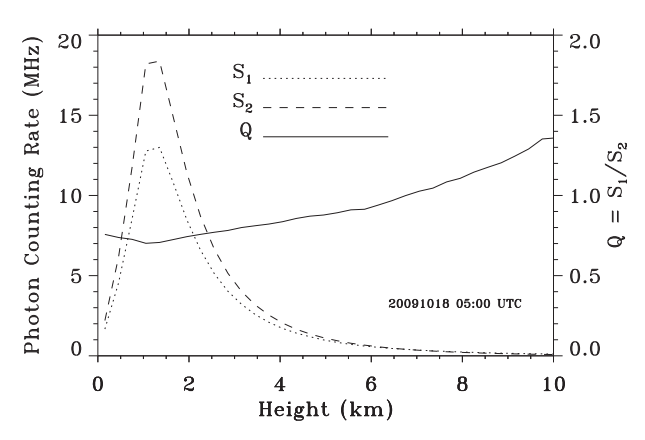


FIG. 4. Representative background-subtracted RR signals from the RR1 (low-J) and RR2 (high-J) detection channels as functions of height. This example is taken from \sim 0500 UTC on 18 October 2009. The signals from the RR1 and RR2 channels are denoted S1 and S2, respectively. The solid line shows the corresponding signal ratio Q. The time and height resolutions are 60 min and 300 m, respectively.

$$T' = T/300 \,\mathrm{K}$$
. (2)

The scale factor of $300 \, \mathrm{K}$ is used simply to make the calibration constant b nondimensional and of the same order of magnitude as a.

Figure 4 shows representative samples of the signals measured by the two RR channels as well as the corresponding signal ratio Q. Both signals reach their maximum value at a height of about 1.5 km AGL. With the exception of the region below this level, the signal ratio increases monotonically. In the region where overlap effects are negligible, the altitude variation in the signal ratio is mainly affected by the variation in atmospheric temperature. For the SGPRL, the overlap effect is significant only in the lowest 4 km of the profile; this is due to the size of the field of view (0.3 mrad). In the region of complete overlap, the signal ratio increases with altitude as the energy in the high-J rotational states decreases relative to the low-J states as a result of decreasing temperature.

3. Raman lidar temperature algorithm

Computing the temperature from Eq. (1) requires the determination of the two calibration coefficients and the overlap function. Once these quantities are established the temperature is computed by simply solving Eq. (1) for T'; that is,

$$T' = \frac{b}{\ln(Q/O) - a}. (3)$$

The essential steps of the RL temperature algorithm include signal preprocessing, calibration, and overlap

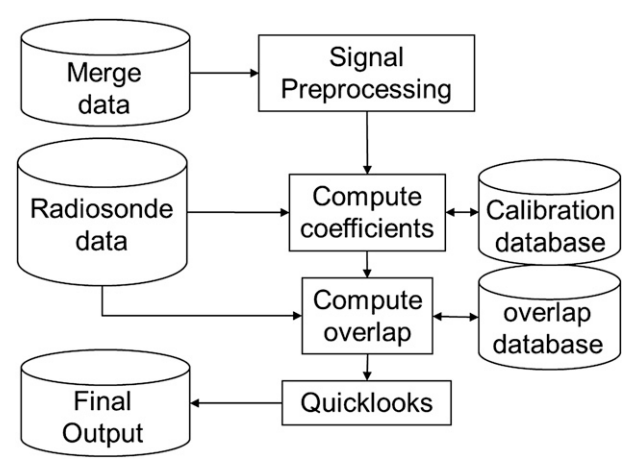


FIG. 5. Flow diagram of the RL temperature algorithm.

correction, as illustrated by the flow diagram in Fig. 5. The details of these steps are described in the following subsections.

a. Preprocessing

The RL temperature algorithm takes input photon counting rate data from the so-called merge algorithm (Newsom et al. 2009), which applies deadtime corrections and combines raw analog-to-digital voltages and deadtime-corrected photon counting data from the transient data recorders using a process referred to as "gluing" (Whiteman et al. 2006). The merge algorithm produces output files containing photon counting rate signals for all of the detection channels in the system. These signals are recorded with a range resolution of 7.5 m and a temporal resolution of 10 s. The RL temperature algorithm first reads in the two RR signals from the merge output and performs a few basic preprocessing operations on the signals. This includes averaging the signals to prescribed time and height bins, background subtraction, and quality control (QC).

Photon counting rate data from merge are first converted to photon counts and then accumulated over user specified time and height bins. The accumulated photon counts are used to compute error estimates of the signal and background and then are converted back into photon counting rates. The average photon counting rate within a given user specified time and height bin is given by

$$\Psi = \left(\frac{c}{2NM\Delta r_{\text{now}}}\right)\psi,\tag{4}$$

where ψ is the accumulated photon count, $\Delta r_{\rm raw}$ is the range resolution of the raw data (7.5 m), and c is the speed of light. The size of the averaging interval is defined by the laser shot count N and the number of raw

range bins accumulated M. For this study, we used M = 40, which gives a height resolution of 300 m for $\Delta r_{\text{raw}} = 7.5 \,\text{m}$. The temporal resolution used in this study was $60 \,\text{min}$, so the laser shot count N was typically on the order of 10^5 .

The background photon counting rate signal within a given user specified time bin is similarly given by

$$\Psi_b = \left(\frac{c}{2NM_b \Delta r_{\text{raw}}}\right) \psi_b, \tag{5}$$

where ψ_b is the accumulated background photon count and M_b is the number of range bins accumulated in the background portion of the raw signal. The background signal is computed by accumulating photon counts over approximately $M_b \sim 300\,\mathrm{raw}$ range bins that are recorded just prior to pulse transmission.

Assuming Poisson statistics, the uncertainties in the average counting rates are given by

$$\delta\Psi = \left(\frac{c}{2NM\Delta r_{\text{raw}}}\right)\sqrt{\psi} \tag{6}$$

for the signal plus background and

$$\delta \Psi_b = \left(\frac{c}{2NM_b \Delta r_{\text{raw}}}\right) \sqrt{\psi_b} \tag{7}$$

for the background. The background-subtracted signal and corresponding uncertainty estimate are given by

$$S = \Psi - \Psi_b \tag{8}$$

and

$$\delta S^2 = \delta \Psi^2 + \delta \Psi_b^2, \tag{9}$$

respectively.

The final preprocessing step involves some basic quality control in which samples are flagged as invalid if they fall below a minimum signal level or are deemed to be cloud contaminated. Samples occurring above estimates of cloud-base height (CBH) or with photon counting rates below 10 kHz were flagged as invalid. The CBH is computed in the merge code by convolving a 6-point Haar wavelet function over profiles of the wide-field-of-view (WFOV) elastic (355 nm) signal. The wavelet detects abrupt increases in the elastic signal with height. Invalid samples are not used in any further processing.

b. Calibration

The calibration coefficients are determined by comparing lidar and radiosonde measurements between

5 and 15 km AGL and for a temperature range of 200 to 320 K. Values falling outside this range are rejected in the calibration procedure. The minimum calibration height of 5 km AGL was chosen to be high enough to ensure complete overlap between the outgoing beam and the field of view of the receiver. For heights above 5 km AGL, the overlap function can be ignored and Eq. (1) can be rewritten as

$$y = a + bx, (10)$$

where $y = \ln Q$ and x is the reciprocal of the normalized temperature. For the purpose of calibration, we set

$$x = 300 \,\mathrm{K/T_{sonde}},\tag{11}$$

where $T_{\rm sonde}$ is the temperature (K) from the radiosonde. Calibrations are performed using only lidar profiles acquired at the time of a given radiosonde launch. The

acquired at the time of a given radiosonde launch. The radiosonde launch site is for all practical purposes collocated with the Raman lidar. Since we are using a relatively long averaging time (60 min), the calibration procedure makes no attempt to account for the horizontal drift of the radiosonde or the time difference between samples in the radiosonde profile. Thus, it is assumed that the radiosonde observations are representative of a single vertical profile over the lidar site during the averaging period of the lidar.

The calibration coefficients, a and b, in Eq. (10) are determined by linear regression, where the uncertainty in y is given by

$$\delta y = |\delta Q/Q|. \tag{12}$$

The uncertainty in Q is in turn computed from

$$(\delta Q/Q)^2 = (\delta S_1/S_1)^2 + (\delta S_2/S_2)^2, \tag{13}$$

where δS_1 and δS_2 are determined from Eq. (9) for their respective channels.

The regression analysis yields estimates of a and b, as well as the corresponding uncertainties δa and δb , respectively. Thus, once the calibration coefficients and uncertainties are determined from the regression analysis, the uncertainty in T is estimated by applying standard error analysis to Eq. (3). The result is given by

$$\left(\frac{\delta T}{T}\right)^2 = T'^2 \left(\frac{\delta Q}{bQ}\right)^2 + T'^2 \left(\frac{\delta a}{b}\right)^2 + \left(\frac{\delta b}{b}\right)^2. \quad (14)$$

¹The radiosonde launch site at the SGP central facility is located about 80 m southwest of the Raman lidar.

Equation (14) accounts for uncertainties in signal ratio Q and the two calibration coefficients, a and b, but does not include any contribution from the uncertainties in the overlap function. Estimating the uncertainties in the overlap function is inherently difficult and so no attempt was made to include it in the overall error estimate of T.

The RL temperature algorithm processes three contiguous 24-h periods on a single call. This includes the date specified in the call and 1 day on both sides of that date. The first step in the calibration process involves reading in the radiosonde temperature data and interpolating these data to the lidar height grid. The next step involves computation of the so-called background calibration coefficients. The background calibration is derived by applying the regression analysis using all simultaneous radiosonde and lidar profiles over the 3-day processing period. In this sense, the background calibration represents an average over the 3-day period. The final step in the calibration procedure involves the computation of time-varying calibration coefficients by repeating the regression analysis for the individual sounding times. In this step, the background calibration is used as a constraint in order to minimize the effect of outliers resulting from noisy variations in individual profiles.

The background calibration coefficients are derived by minimizing the cost function

$$L_o = \sum_{ij} \frac{(y_{ij} - a_o - b_o x_{ij})^2}{\delta y_{ii}^2}$$
 (15)

with respect to a_o and b_o . The summation in Eq. (15) is over all heights z_j and sounding times t_i during the 3-day processing period. Applying the standard least squares procedure results in the following 2×2 linear system:

$$\mathbf{A}_{o} \begin{pmatrix} a_{o} \\ b_{o} \end{pmatrix} = \mathbf{f}_{o}, \tag{16}$$

where

$$\mathbf{A}_{o} = \sum_{ij} \delta y_{ij}^{-2} \begin{pmatrix} 1 & x_{ij} \\ x_{ij} & x_{ij}^{2} \end{pmatrix}$$
 (17)

and

$$\mathbf{f}_o = \sum_{ij} \delta y_{ij}^{-2} \begin{pmatrix} y_{ij} \\ x_{ij} y_{ij} \end{pmatrix}. \tag{18}$$

The solution of Eq. (16) is readily obtained using standard methods. Estimates of the errors in a_o and b_o are given by

$$\delta a_o = (\mathbf{A}_o^{-1})_{11} \tag{19}$$

and

$$\delta b_o = (\mathbf{A}_o^{-1})_{22}. \tag{20}$$

(Press et al. 1988). Figure 6 shows a representative example of the background calibration regression analysis. This particular example was obtained using 3 days of lidar and radiosonde observations (i.e., 12 comparisons) centered on 5 January 2009. The straight-line fit is obtained through samples for which 5 km < z < 15 km and $200 \, {\rm K} < T_{\rm sonde} < 320 \, {\rm K}$. The offset and slope of this fit determine a_o and b_o , respectively.

Once the background calibration coefficients have been established, the temporal variation in the calibration is estimated by repeating the regression analysis for individual sounding times, while imposing the background calibration as a weak constraint. In this case, the cost function is given by

$$L_{i} = \lambda \sum_{j} \frac{(y_{ij} - a_{i} - b_{i}x_{ij})^{2}}{\delta y_{ij}^{2}} + \lambda_{o} \left[\frac{(a_{i} - a_{o})^{2}}{\delta a_{o}^{2}} + \frac{(b_{i} - b_{o})^{2}}{\delta b_{o}^{2}} \right], \tag{21}$$

where a_i and b_i are estimates of the calibration coefficients corresponding to specific sounding times t_i . The summation in Eq. (21) is performed only in the height dimension for a specific sounding time. The weighting parameters λ and λ_o are used to control relative contribution between the *i*th sounding and the background. In this study, the weighting parameters were fixed at $\lambda = \lambda_o = 1$. Minimization of Eq. (21) yields the following linear system:

$$\mathbf{A}_{i} \begin{pmatrix} a_{i} \\ b_{i} \end{pmatrix} = \mathbf{f}_{i}, \tag{22}$$

where

$$\mathbf{A}_{i} = \lambda \sum_{j} \delta y_{ij}^{-2} \begin{pmatrix} 1 & x_{ij} \\ x_{ij} & x_{ij}^{2} \end{pmatrix} + \lambda_{o} \begin{pmatrix} \delta a_{o}^{-2} & 0 \\ 0 & \delta b_{o}^{-2} \end{pmatrix}$$
(23)

and

$$\mathbf{f}_{i} = \lambda \sum_{i} \delta y_{ij}^{-2} \begin{pmatrix} y_{ij} \\ x_{ij} y_{ij} \end{pmatrix} + \lambda_{o} \begin{pmatrix} a_{o} / \delta a_{o}^{2} \\ b_{o} / \delta b_{o}^{2} \end{pmatrix}. \tag{24}$$

Once again, the solution to Eq. (22) is obtained using standard methods, and the uncertainties in a_i and b_i are estimated from

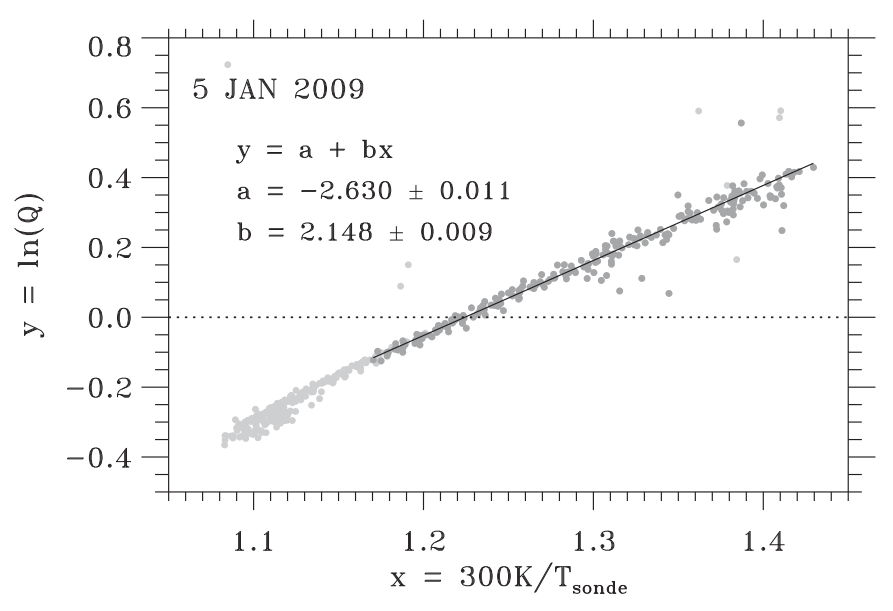


FIG. 6. Background calibration regression analysis for a 3-day period centered on 5 Jan 2009. Dark gray dots are samples that are used in the regression analysis (i.e., samples for which $5\,\mathrm{km} < z < 15\,\mathrm{km}$ and $200\,\mathrm{K} < T_\mathrm{sonde} < 320\,\mathrm{K}$). Light gray dots are samples that fall outside this range. The solid black curve is the fit through the dark gray dots.

$$\delta a_i = (\mathbf{A}_i^{-1})_{11} \tag{25}$$

and

$$\delta b_i = (\mathbf{A}_i^{-1})_{22}. \tag{26}$$

Once the calibration coefficients and uncertainties have been estimated, they are subjected to a quality assurance (QA) test. If

$$\sqrt{(\delta a_i/a_i)^2 + (\delta b_i/b_i)^2} \le 0.03,$$
 (27)

then the coefficients are used for calibration and saved to a database file for possible use on other days. If none of the calibration coefficients pass the QA test, then the algorithm searches the database file for coefficients from a date closest to the specified processing date.

The procedure outlined above produces estimates of the calibration coefficient and their uncertainties at the sounding times t_i . These quantities are then linearly interpolated to the sample times of the lidar profiles. We note that typically four radiosondes are launched every day at the SGP central facility. The RL temperature algorithm uses a 3-day sliding window to estimate temperature profiles for the middle day, so that the interpolation is typically performed using 12 sample pairs of calibration coefficients. Thus, this scheme eliminates artifacts associated with interpolation end effects for the

middle day and helps to improve the continuity between consecutive days.

c. Overlap correction

The height dependence of the RR signal ratio in the lowest 2 to 3 km of the atmosphere is dominated by the effects of incomplete overlap between the receiver and the outgoing laser beam cross section. If this effect is not accounted for, the error in the derived temperature profile below about 3 km can be quite large.

Given the sensitivity of the results to the specification of the overlap function in the lowest $3\,\mathrm{km}$ of the temperature profile, the algorithm imposes multiple levels of QA. The first step in this process involves estimating the overlap function for the specified date using simultaneous measurements of Q and T_{sonde} . As in the calibration procedure, 3 days of observations are used to estimate the overlap function for the middle day.

Using Eq. (1), a rough estimate of O(z) is obtained from

$$\tilde{O}(z) = \langle Q/\exp(a_i + b_i x) \rangle,$$
 (28)

where $\langle \cdot \rangle$ denotes a median at a fixed height over all radiosonde times t_i . The median profile is computed using 3 days of observations, which typically includes 12 radiosonde profiles at the SGP central facility.

The result from Eq. (28) can exhibit significant variability with height due to measurement noise. In theory,

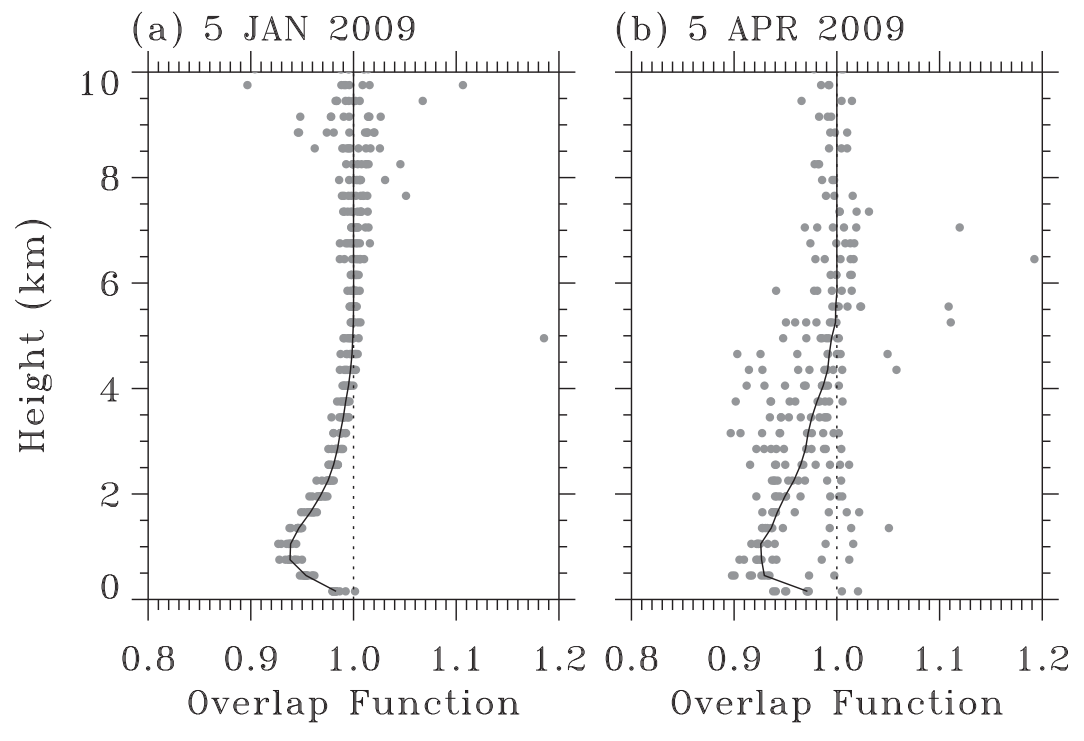


FIG. 7. Representative examples of overlap function determined for (a) 5 Jan 2009 and (b) 5 Apr 2010. Gray dots are individual samples of $Q/\exp(a + bx)$ and the solid black lines are estimates of O(z).

the overlap function should be a smoothly varying function of height that asymptotically approaches one as z becomes large. To further suppress any residual random variability with height, $\tilde{O}(z)$ is subjected to a 3-point boxcar smoothing filter; that is,

$$\hat{O}(z_j) = [\tilde{O}(z_{j-1}) + \tilde{O}(z_j) + \tilde{O}(z_{j+1})]/3.$$
 (29)

To force the result to a constant value of one at large z, $\hat{O}(z)$ is linearly blended with a function w(z) that varies smoothly from 0 for z less than 4 km to 1 for z greater than 6 km. The final estimate of the overlap function for a specific date is given by

$$O(z) = [1 - w(z)]\hat{O}(z) + w(z). \tag{30}$$

The result from Eq. (30) is then compared to a "standard" overlap function, which is determined through offline analysis and stored in a configuration file. The standard overlap function is derived based on several weeks of observations using a procedure similar to that described above. If the coefficient of linear correlation between O(z) and the standard overlap function is greater than 0.8 and the RMS difference is less than 0.01, then O(z) is saved to a database file and used in the determination of the temperature. If the above QA condition is not met, then the algorithm searches the

database file for an overlap function from a date closest to the specified processing date.

In contrast to the calibration procedure, no attempt is made to estimate the temporal variation of the overlap function during the specified date. The procedure outlined above produces an overlap function that represents an average over 3 days of observations. Although the variation from day to day is typically quite small, there are instances when the overlap function changes abruptly because of sudden changes in optical alignment. In these relatively rare cases, errors will result in the temperature profiles at lower altitudes.

Figure 7 shows representative examples of overlap functions obtained using the procedure outlined above. Gray circles represent individual samples of $Q/\exp(a+bx)$, and the solid black lines are the estimates of O(z). Figure 7a shows a case in which there is little scatter in the individual samples of $Q/\exp(a+bx)$, and Fig. 7b shows a less well-behaved case in which the scatter is more significant. In both of these cases, the estimated overlap functions passed the QA test.

d. Estimated uncertainty

Figure 8 shows profiles of the median absolute (Fig. 8a) and relative uncertainties (Fig. 8b) in *T* as computed from Eq. (14). We emphasize that these profiles represent estimates based largely on the effects of shot noise.

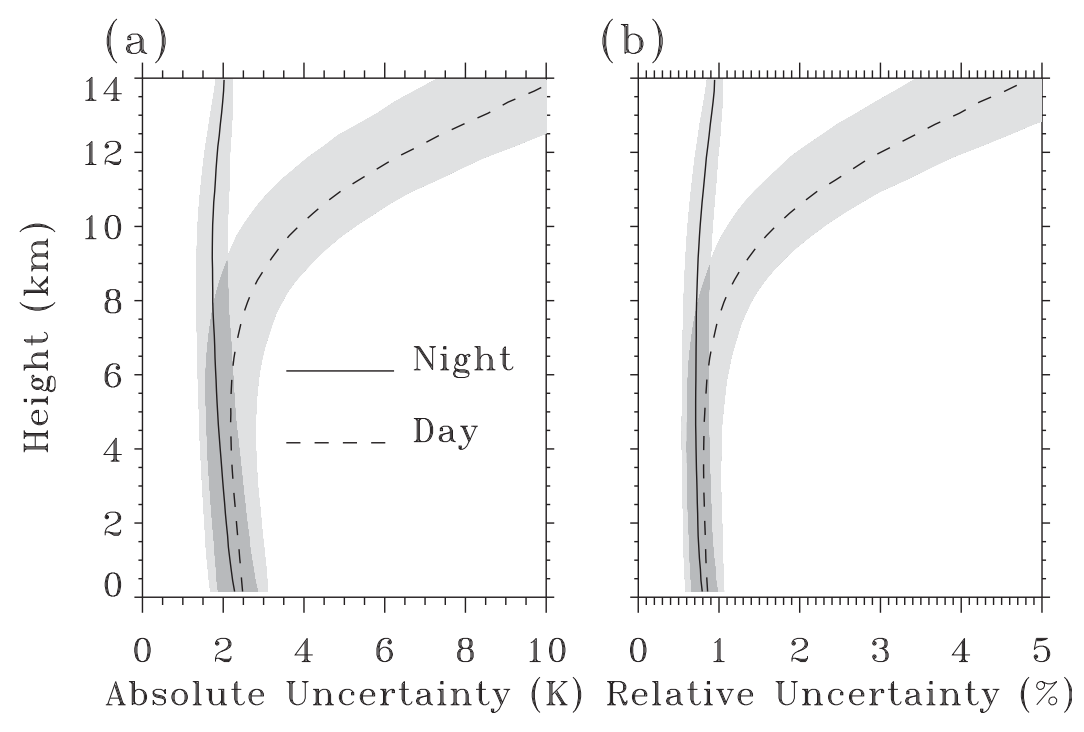


FIG. 8. Profiles of the median (a) absolute and (b) relative uncertainties in the lidar-derived temperature during nighttime (solid) and daytime (dashed). The shaded regions indicate the range of values between the 25th and 75th percentiles.

The profiles in Fig. 8 were obtained using a temporal resolution of 60 min and a constant height resolution of 300 m and are broken down in terms of nighttime and daytime uncertainties based on the strength of the total solar background signal (i.e., the sum of the background signals from the two RR channels). The night-time cases correspond to total solar background levels below 10 kHz, and the daytime cases correspond to levels above 100 kHz. Statistics were computed using 7723 nighttime profiles and 7858 daytime profiles over the 2-yr period from 1 January 2009 to 31 December 2010.

Equation (14) indicates that the height dependence of the temperature uncertainty is determined by the temperature and the uncertainty in the signal ratio Q. Although the uncertainty in Q increases monotonically with heights above $1 \, \mathrm{km} \, \mathrm{AGL}$ (not shown), the temperature uncertainty estimate can remain constant or even decrease with height because of the decreasing temperature. Figure 8b shows that during the nighttime the median relative uncertainty below $5 \, \mathrm{km} \, \mathrm{AGL}$ is approximately constant at about 0.8%; it then increases slowly to about 1% at $15 \, \mathrm{km} \, \mathrm{AGL}$. The daytime median relative uncertainty is also approximately constant at about 0.9% below $5 \, \mathrm{km} \, \mathrm{AGL}$; it then increases sharply above $6 \, \mathrm{km} \, \mathrm{AGL}$ to about 5% at $14 \, \mathrm{km} \, \mathrm{AGL}$.

The larger daytime uncertainty is due to the effects of solar radiation in the measurement. Near solar noon the strength of the solar background from the RR1 (low-J) channel varies between roughly 0.5 and 1 MHz from winter to summer, respectively. Over this same period, the solar background from the RR2 (high-J) channel varies between roughly 1.5 and 3 MHz.

On average, we find that the direct contribution from shot noise to the total uncertainty, as given by the first term in Eq. (14), is roughly 15%. The largest contribution to the error budget comes from the estimation error in the calibration coefficients. These estimation errors are derived from least squares fits in which the measurement uncertainty is determined from shot noise, as given by Eq. (12). Thus, the uncertainties in the calibration coefficients are themselves dependent upon the shot noise.

4. Accuracy and calibration stability

The accuracy of the lidar temperature profiles is evaluated by comparison with radiosonde measurements over the 2-yr period from 1 January 2009 to 31 December 2010. Unless otherwise stated, all statistical results presented in this section were computed using only clear-sky profiles. Also, only lidar estimates below a relative

TABLE 2. Daily radiosondes used for calibration and overlap correction for each of the run types. Check marks indicate calibration soundings and dashes indicate noncalibration soundings. Also shown are the height and time resolutions for each run type.

Calibration radiosondes (UTC)					Resolution	
Run type	0530	1130	1730	2330	Δz (m)	$\Delta t \text{ (min)}$
1	1	~	/	~	300	60
2		_	_	_	300	60
2a		_	_	_	300	60

uncertainty of 10%, as determined from Eq. (14), were used in the comparisons.

The RL temperature algorithm was run using two different configurations, or run types, as listed in Table 2. For run type 1, the lidar temperature measurements were calibrated and overlap corrected using all four daily radiosondes. Thus, the calibration coefficients for run type 1 are updated once every 6 h. By contrast, both run types 2 and 2a use only the 0530 UTC sounding from each day for calibration and overlap correction. Additionally, run type 2a applies a solar background-dependent correction, which is explained in more detail in section 4e.

The results from run type 1 are used to assess the performance of the calibration and overlap correction procedures and to analyze the long-term, seasonal, and diurnal stability of the calibration. For run types 2 and 2a, the noncalibration soundings provide an independent source of temperature measurements against which the lidar data can be compared. Here, the term noncalibration sounding refers to any radiosonde profile that was not used for the calibration of the lidar.

a. Lidar operational status

During the 2-yr period from 1 January 2009 to 31 December 2011, the SGPRL was operational approximately 95% of the time, as indicated in Fig. 1. The most significant periods of instrument downtime occurred in April 2009, late December 2009, early June 2010, and August of 2010.

Laser problems and associated troubleshooting efforts resulted in downtime in April 2009. In late December 2009, the system was down because of a malfunction in the laser cooling system. Power interruptions and a malfunction in one of the uninterruptable power supplies caused downtime in June 2010, and in August 2010 the system was down on several occasions because of power interruptions and a malfunction of the heating, ventilation, and air-conditioning (HVAC) system.

There were also two periods when the raw signals exhibited anomalous behavior, possibly due to malfunctions

in the automated alignment process. These periods were identified by visual inspection and not included in the comparisons. This included the period from 24 to 26 July 2010 and 21 to 25 October 2010. We note, however, that the statistical results presented in sections 4c through 4e were almost completely unaffected by the inclusion or rejection of these two periods.

b. Radiosondes

The ARM program launches Vaisala RS92 radiosondes from each of its facilities. These radiosondes use a thin capacitive wire element for temperature sensing. This sensor has a measurement range of -90° to $+60^{\circ}$ C, an absolute accuracy of better than 0.5° and reproducibility of 0.2° for altitudes lower than $100 \,\mathrm{mb}$, and a response time of better than 1s for altitudes below $100 \,\mathrm{mb}$ (Vaisala 2010). Comparisons of the RS92 temperature sensor (which is the same sensor as that used on the earlier RS90 radiosonde) with other radiosonde types and models have demonstrated that the RS92 temperature measurement is the most accurate (Luers 1997; Steinbrecht et al. 2008).

c. Run type 1

Figure 9 shows representative examples of potential temperature time-height cross sections for run type 1 (Table 2). The lidar data were calibrated and overlap corrected using the procedures outlined in section 3, and the potential temperature was computed using pressure measurements from radiosondes, which were interpolated between sounding times. The examples include time-height cross sections from 4 months during the 2-yr comparison period and include January 2009, June 2009, April 2010, and October 2010. Data voids in Fig. 9 correspond to regions where measurement uncertainties exceed 10%, as estimated from Eq. (14). In most cases, this occurred as a result of attenuation from clouds. Measurements exceeding 10% relative uncertainty were excluded from the comparisons.

Figure 10 shows profiles of the median and RMS difference between the lidar and radiosonde temperatures from run type 1. The solid curves show results using all clear-sky soundings between 1 January 2009 and 31 December 2010, and the shaded region in Fig. 10a indicates the range of values between the 25th and 75th percentiles of the difference. The median difference profile is approximately constant with height. When averaged vertically for $z < 10\,\mathrm{km}$ AGL, the overall median difference is $0.02\,\mathrm{K}$. These results show very good agreement between the lidar and radiosonde temperature profiles and indicate that the calibration and overlap correction procedures work well.

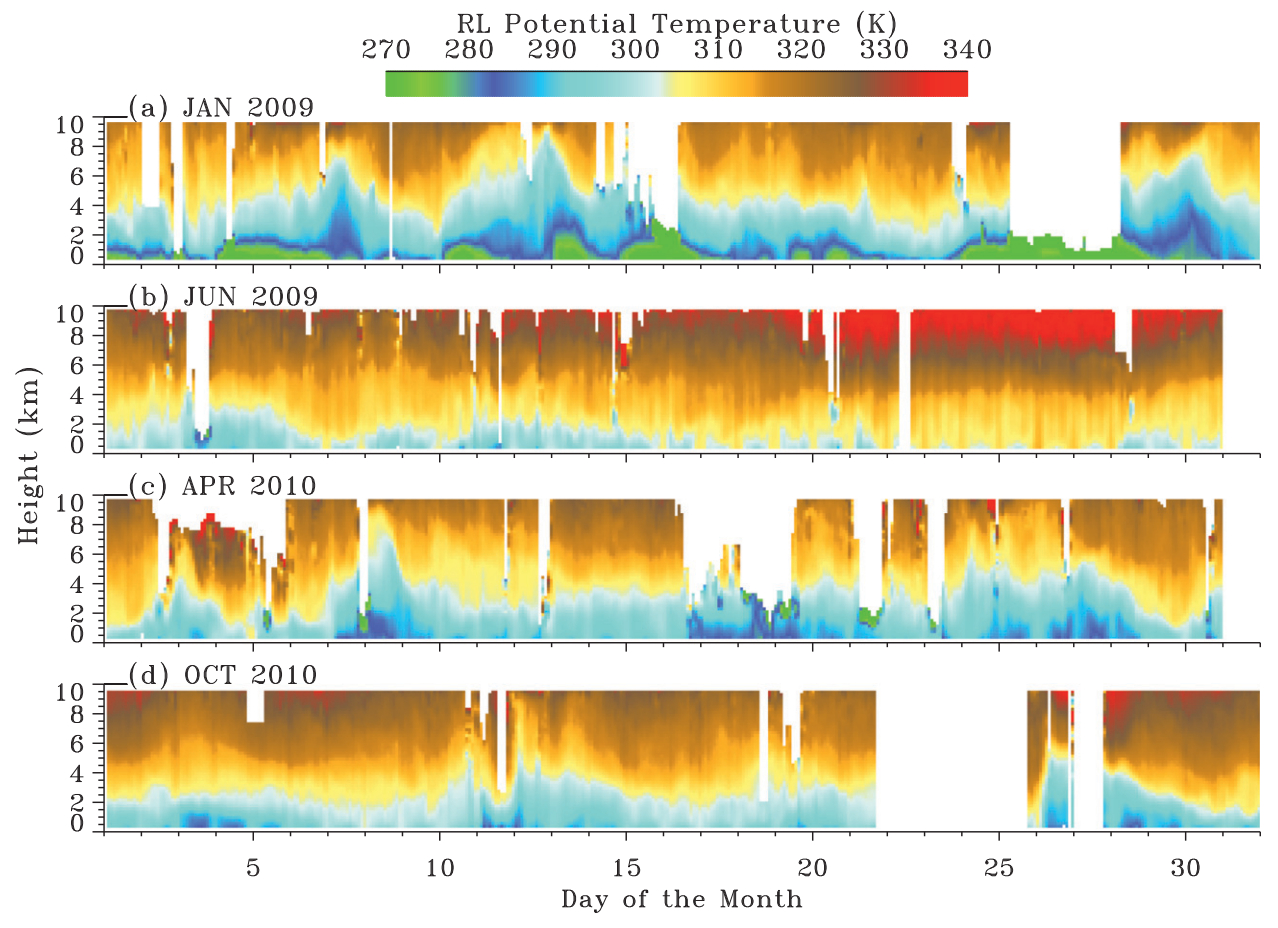


Fig. 9. Time-height cross sections of the lidar-derived potential temperature for (a) January 2009, (b) June 2009, (c) April 2010, and (d) October 2010.

Profiles of the RMS difference between the lidar and radiosonde exhibit different behavior depending upon the sounding time. Figure 10b shows results for the 0530 UTC (dashed–dotted) and 1730 UTC (dashed) sounding times. The nighttime profile (0530 UTC), which is nominally about 1 K, decreases slightly with height before increasing gradually above 5 km AGL. By contrast, the daytime profile (1730 UTC) increases sharply above 5 km AGL. The height dependence of the daytime and nighttime RMS profiles is similar to the uncertainty profiles shown in Fig. 8.

To examine long-term and seasonal calibration stability, Fig. 11 shows a time series of the calibration coefficients over the 2-yr study period, from 1 January 2009 to 31 December 2010. Both a and b show 2% standard deviations relative to their respective 2-yr mean values. There is no obvious long-term or seasonal variation. However, a closer inspection reveals a distinctive diurnal variation in both a and b.

The diurnal variation in the calibrations was investigated by examining the deviation of a and b relative to

their respective diurnal means. These quantities are given by

$$\Delta a_{\rm rel} = (a - \overline{a})/\overline{a} \tag{31}$$

and

$$\Delta b_{\rm rel} = (b - \overline{b})/\overline{b},$$
 (32)

where the overbars denote the daily mean values. Figure 12 shows the relative diurnal variation in *a* and *b* averaged over the period from 1 May to 31 July 2009. We emphasize that calibrations are only obtained at the radiosonde sounding times, as indicated by the dashed vertical lines in Fig. 12. Calibrations between these sounding times are estimated by applying a simple linear interpolation between the sounding times.

Figure 12 clearly shows that both a and b exhibit small but distinct diurnal variations. Both $\Delta a_{\rm rel}$ and $\Delta b_{\rm rel}$ exhibit extremum at the 0530 and 1730 UTC sounding

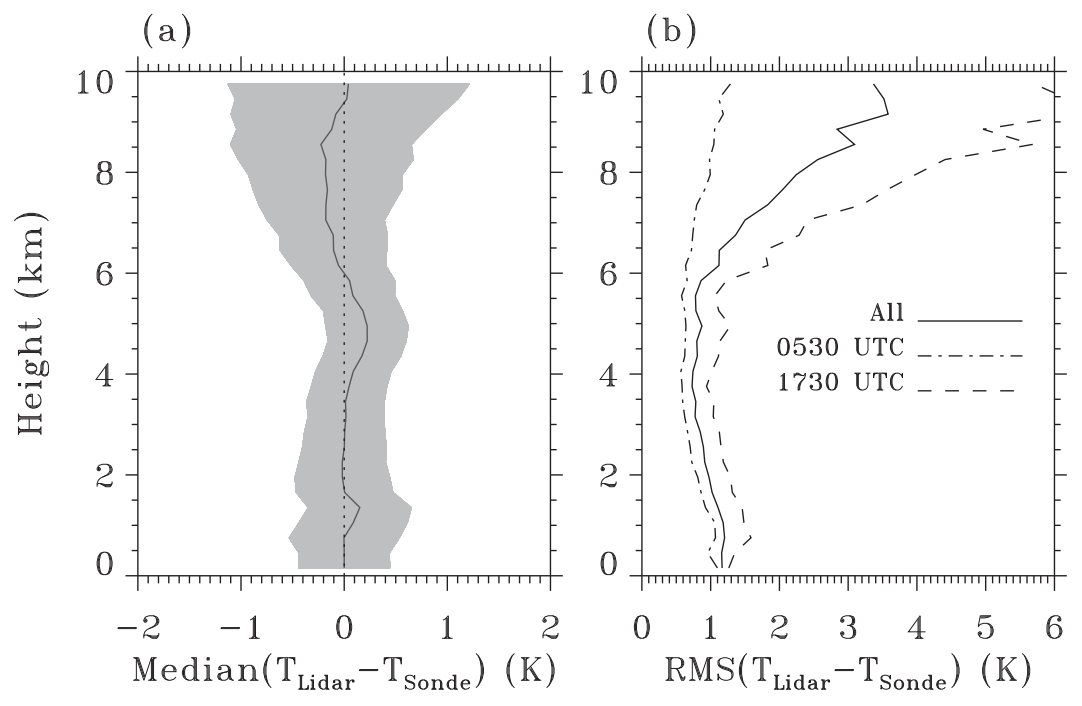


FIG. 10. (a) Median and (b) RMS difference profiles between the lidar and radiosonde temperatures for Run Type 1. The solid curves show results for all radiosonde launch times using 1752 clear-sky soundings between 1 Jan 2009 and 31 Dec 2010. The shaded region in (a) indicates the range of values between the 25th and 75th percentiles of this difference. The dashed and dashed–dotted profiles in (b) are the RMS differences averaged over the 1730 and 0530 UTC sounding times, respectively.

times. The total change in a from minimum to maximum is about 0.4%, and the total change in b from minimum to maximum is about 0.25%. Also shown in Fig. 12 is the mean diurnal solar background, as given by the sum of the two RR signals. There is a clear correlation, or anticorrelation, between the calibration coefficients and the solar background signal, with the largest differences occurring between the nighttime sounding at 0530 UTC and the sounding near solar noon at 1730 UTC.

Although the diurnal variations in the calibration coefficients are small, we note that a 0.4% variation in either of the two calibration coefficients results in a relative variation in temperature of similar magnitude based on Eq. (14). Thus, if the calibrations determined from the 0530 UTC sounding were applied throughout the entire 24-h period, Eq. (14) predicts an error on the order of 1 K at a temperature of 300 K near solar noon.

d. Run type 2

Figure 13 shows profiles of the median difference between the lidar and radiosonde temperatures for run type 2 (Table 2). The solid and dashed curves show the results for the calibration and noncalibration soundings, respectively. These results were derived using profiles acquired under clear-sky conditions between 1 January

2009 and 31 December 2010. There were 462 calibration soundings and 1250 noncalibration soundings used to compute the profiles. The median difference profile for the calibration soundings fluctuates about zero with relatively small values ranging between roughly ± 0.4 K. The shape of this curve is similar to that obtained for run type 1, as shown in Fig. 10. The overall median difference for z < 10 km AGL is essentially 0 K (3×10^{-5} K) for the calibration soundings and 0.84 K for noncalibration soundings.

Figure 14 shows the diurnal variation in the overall median difference between the lidar and radiosonde temperature for run type 2. The differences were computed for $z < 10 \,\mathrm{km}$ AGL and for the period from 1 May to 31 July 2009. Biases for the noncalibration soundings (1130, 1730, and 2330 UTC) all show a warm bias, with a maximum value of 2.4 K occurring at 1730 UTC. By contrast, the bias for the calibration sounding (0530 UTC) is very small. Also shown in Fig. 14 is the mean diurnal variation in the solar background as obtained from the sum of the RR channels. The correlation between the solar background signal and the lidar bias is clear. We note that the variations shown in Fig. 14 are representative of a 3-month period spanning the summer solstice. The variation is less extreme during the winter months.

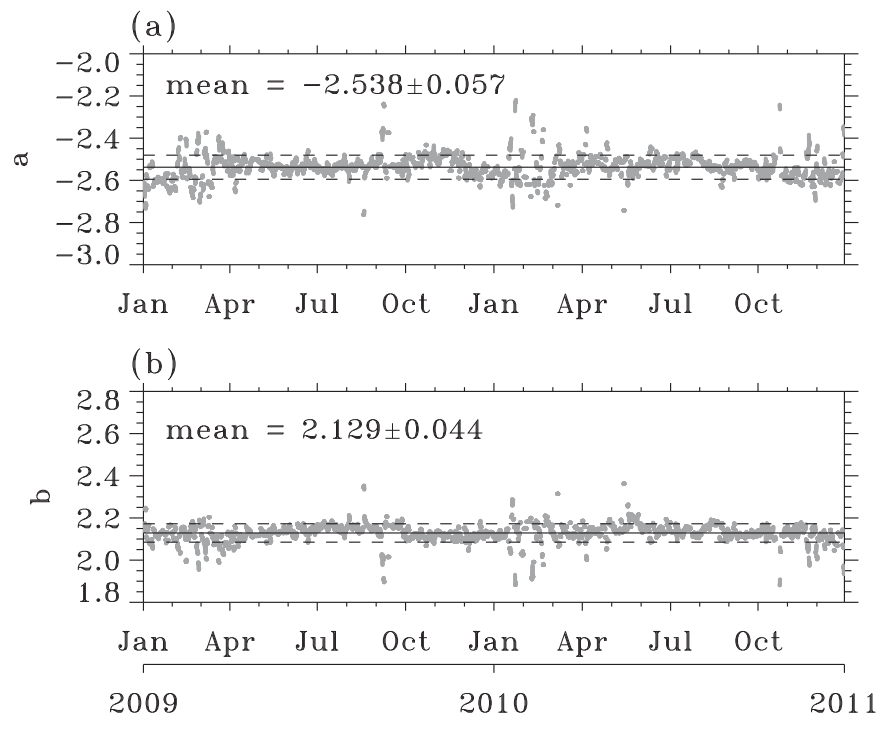


FIG. 11. Time series of (a) *a* and (b) *b* over a 2-yr period from 1 Jan 2009 to 31 Dec 2010. The means and standard deviations are indicated by the solid and dashed lines, respectively.

e. Run type 2a

Results from run type 1 showed that the calibration coefficients exhibit a small diurnal variation and that this variability is correlated with the strength of the solar background signal. Results from run type 2 essentially showed that when this diurnal variability is not resolved, the lidar temperature data exhibit significant diurnally dependent biases.

In cases where the frequency of radiosonde measurements is not sufficient enough to resolve the diurnal variation, it is desired to develop methods to estimate the variation between calibration periods. Given the clear correlation between the solar background and the calibration, the approach adopted here involves parameterizing the calibration coefficients in terms of the observed solar background level, thereby enabling a means of correcting the calibrations between calibration soundings.

Figure 15 shows scatterplots of $\Delta a_{\rm rel}$ and $\Delta b_{\rm rel}$ versus the natural log of the total solar background signal

$$f = \ln(S_b), \tag{33}$$

as obtained from run type 1 results. Although the scatter is significant, there is a clear trend that is well represented by straight-line fits, as indicated in Fig. 15. The results shown in Fig. 15 were obtained using

1136 calibration soundings between 1 April 2009 and 31 August 2009. This period was chosen because it spans the summer solstice and corresponds to a time of the year when the diurnal variation in the lidar bias is the most pronounced. For run type 2a (Table 2), the straight-line fits shown in Fig. 15 were used to develop a simple relationship between the calibration coefficients and the observed total solar background signal. The parameterization for *a* is given by

$$a(f) = a(f_o) \left[1 + (f - f_o) \frac{\partial \Delta a_{\text{rel}}}{\partial f} \right], \tag{34}$$

where f_o is obtained by linearly interpolating f between calibration times, and $\partial \Delta a_{\rm rel}/\partial f$ is given by the slope of the straight-line fit shown in Fig. 15a. Likewise, the parameterization for the b is given by

$$b(f) = b(f_o) \left[1 + (f - f_o) \frac{\partial \Delta b_{\text{rel}}}{\partial f} \right], \tag{35}$$

where $\partial \Delta b_{\rm rel}/\partial f$ is given by the slope of the straight-line fit shown in Fig. 15b.

Equations (34) and (35) are used to make small adjustments to a and b between calibration times. The calibration coefficients determined from the calibration soundings are denoted by $a(f_o)$ and $b(f_o)$. As before,

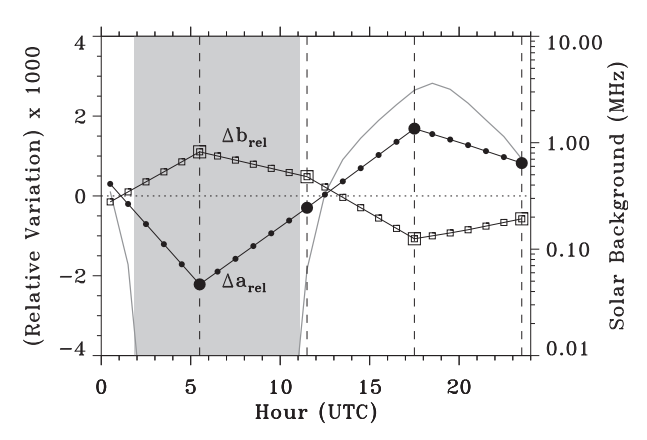


FIG. 12. Mean relative diurnal variation in *a* and *b* based on an average over a 3-month period from 1 May to 31 Jul 2009. Radiosonde sounding times are indicated by the dashed vertical lines. The total solar background (summed from RR1 and RR2) is shown by the gray curve and the nighttime period is indicated by the gray shaded area.

these quantities are obtained by linear interpolation between calibration times. The strength of the correction depends on the instantaneous difference between f and f_o . As a result, the calibrations are only modified between calibration sounding times. If $\partial \Delta a_{\rm rel}/\partial f$ and $\partial \Delta b_{\rm rel}/\partial f$ are

both set to zero, this scheme reduces to the original process.

Run type 2a was set up to use the above scheme with $\partial \Delta a_{\rm rel}/\partial f = 4.8 \times 10^{-4}$ and $\partial \Delta b_{\rm rel}/\partial f = -2.8 \times 10^{-4}$, as indicated in Fig. 15. As in run type 2, only the 0530 UTC radiosondes were used for calibration and overlap correction.

Figure 16 shows the diurnal variation in the overall temperature bias for run type 2a. Comparing these results to those for run type 2 (Fig. 14) shows a significant reduction in the bias during the noncalibration sounding times (1130, 1730, and 2330 UTC). Similarly, Fig. 17 shows profiles of the median and RMS difference between the lidar and radiosonde temperature profiles for run type 2a using all noncalibration soundings. Comparing the bias profile of Fig. 17 to the corresponding result for run type 2 (dashed curve in Fig. 13) shows a marked improvement. The overall median bias for z <10 km AGL is 0.005 K. The RMS difference fluctuates about 2K below about 6km AGL and then increases sharply to roughly 4.5 K at a height of 10 km AGL. The RMS difference is larger than for run type 1 (Fig. 10b), but this is not surprising since the results shown in Fig. 17 represent comparisons between independent temperature measurements. By contrast,

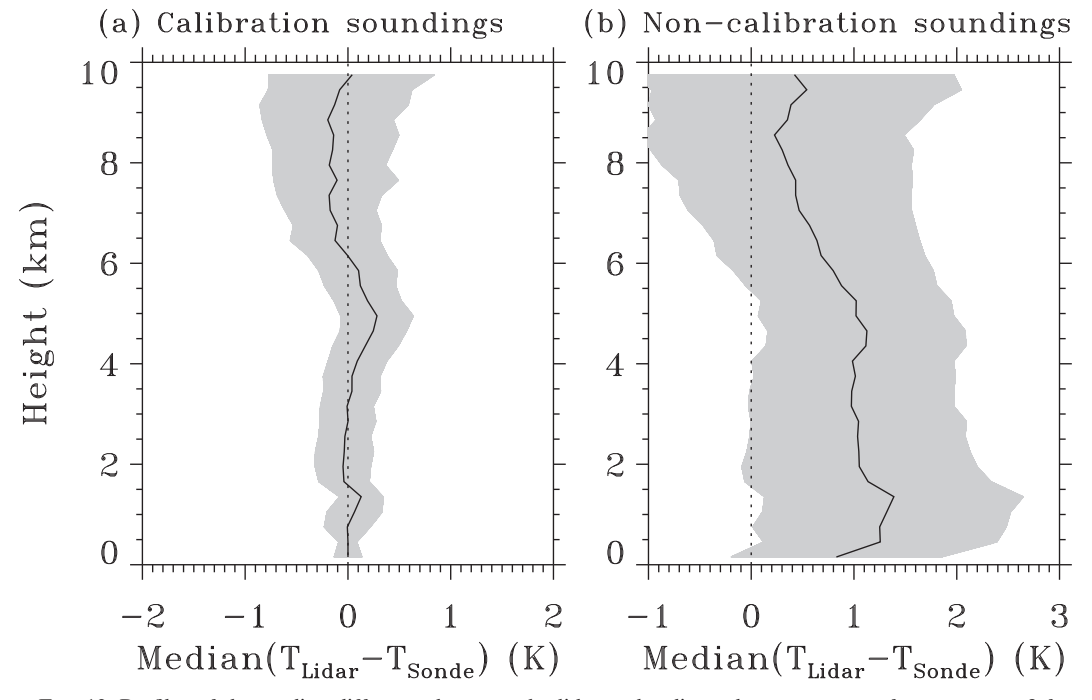


FIG. 13. Profiles of the median difference between the lidar and radiosonde temperatures from run type 2 for (a) calibration soundings and (b) noncalibration soundings. Statistics were derived using profiles acquired under clear-sky conditions between 1 Jan 2009 and 31 Dec 2010. There were 462 calibration soundings and 1250 noncalibration soundings used. The overall median difference is $3 \times 10^{-5} \, \mathrm{K}$ for the calibration soundings and 0.84 K for the noncalibration soundings. The shaded regions indicate the range of values between the 25th and 75th percentiles of the differences.

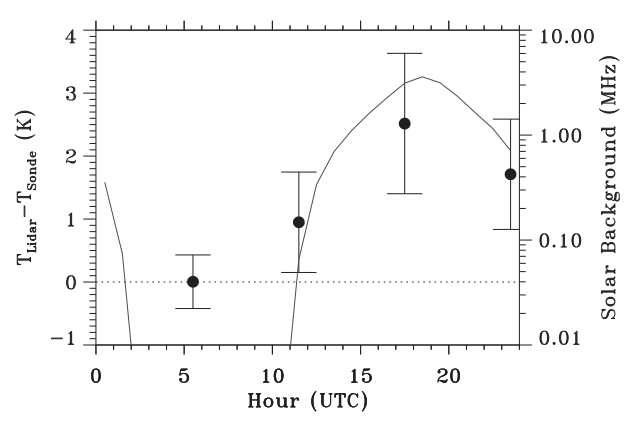


FIG. 14. Median difference between the lidar and radiosonde temperatures for run type 2. Results were computed using all clear-sky profiles between 1 May and 31 Jul 2009 and for heights below 10 km AGL. Error bars indicate the range of values between the 25th and 75th percentiles. The total solar background (summed from RR1 and RR2) is shown by the gray curve.

the lidar temperature profiles used in Fig. 10 are strongly dependent on the radiosonde measurements.

The results for run type 2a demonstrate that the correction scheme described above is effective at reducing the lidar temperature biases between calibration sounding times. Such a scheme can easily be used in

cases where the calibrations are performed infrequently, provided the dependence of the calibration coefficients on the solar background can first be characterized. In this case the slope parameters, $\partial \Delta a_{\rm rel}/\partial f$ and $\partial \Delta b_{\rm rel}/\partial f$, were determined using a subset of the data and then applied to the entire 2-yr period. We note that the effect of the correction is most pronounced during the summer months when the diurnal variation in the solar background is largest.

f. Signal nonlinearity

Possible causes for the observed diurnal variation in calibration include nonlinearities in the RR photon counting rate signals and/or effects induced by thermal cycling within the lidar enclosure. Thermal stability of the enclosure could affect alignment, laser frequency, and filter characteristics. The temperature inside the lidar enclosure does in fact exhibit a small diurnal variation of about $\pm 0.5^{\circ}$ C; however, this relatively small fluctuation is not expected to have a significant impact on the laser frequency or the filter pass bands. Furthermore, the temperature fluctuation lags the variation in the solar background by several hours; whereas our results indicate that the fluctuation in calibration is in phase with the solar background (see Fig. 12). Although we cannot completely rule out thermal effects, our

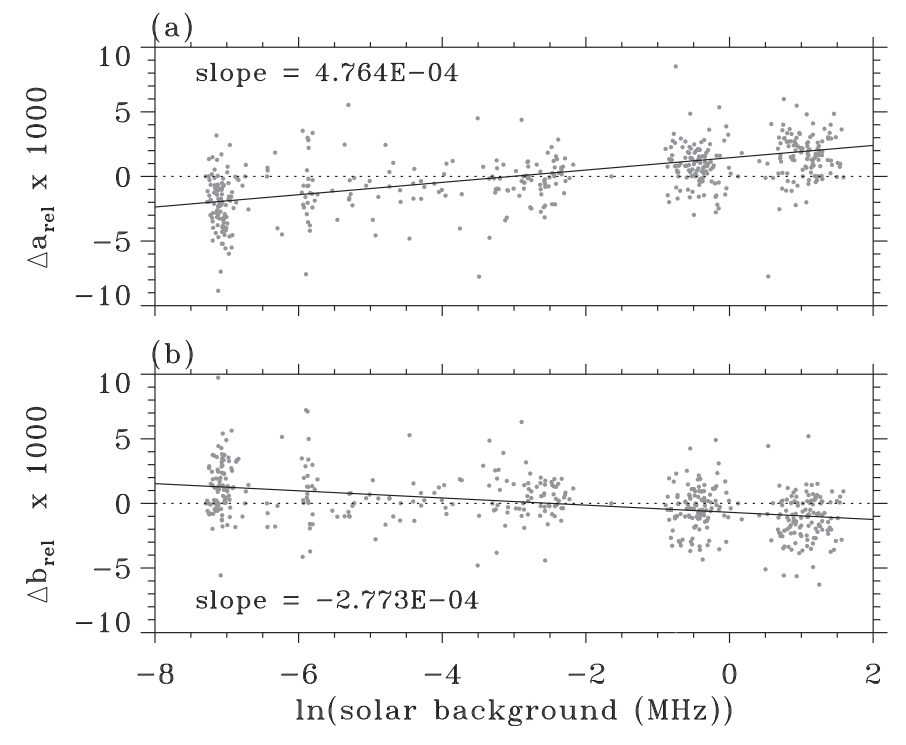


FIG. 15. Gray dots show the deviation of (a) a and (b) b relative to their respective daily mean values as functions of the natural log of the total solar background. The solid black curves represent straight-line fits.

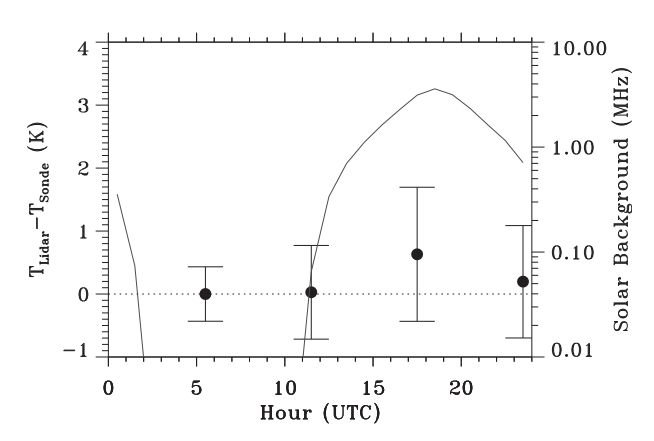


FIG. 16. As in Fig. 14, but for run type 2a.

results suggest that this may not be the main cause for the observed behavior.

Instead, we believe that residual nonlinearities in the RR signals are the likely cause of the diurnal variation in calibration. To test this hypothesis, we examined the relationship between the deadtime-corrected photon counting rate and the analog voltage measurements for the two RR detection channels. Although the analog measurements lack the sensitivity of the photon counting rate data, they exhibit superior linearity. As discussed in section 3a, the raw photon counting rate data

are corrected for deadtime (i.e., pulse pile-up) effects. The correction, which uses the standard nonparalyzable equation (Whiteman et al. 2006), is effective at removing much of the nonlinearity, but some residual nonlinearity does remain. In our implementation of the gluing procedure, scaled analog data are used when the deadtime-corrected photon counting rate exceeds a threshold of 20 MHz. In the case of the RR signals, the maximum counting rate rarely exceeds this threshold. Thus, the signals used in this study are almost completely composed of deadtime-corrected photon counting rate data.

Figure 18 shows plots of the median analog voltage versus the (deadtime corrected) photon counting rate for the two RR channels. These plots were obtained from a total of about 34 000 profiles (10-s time resolution) spanning 4 days of measurements (25, 26, 29, and 30 June 2012) and using only measurements within the calibration height range of 5 to 15 km AGL. In this height range, the RR signals are typically less than 2 MHz above the background level. As the solar background increases, the calibration band shifts to higher photon counting rates.

Both the curves for RR1 and RR2 shown in Fig. 18 exhibit slight curvatures. This implies a slight nonlinearity in the response of the measured photon counting rates, assuming the analog voltage varies linearly with the true

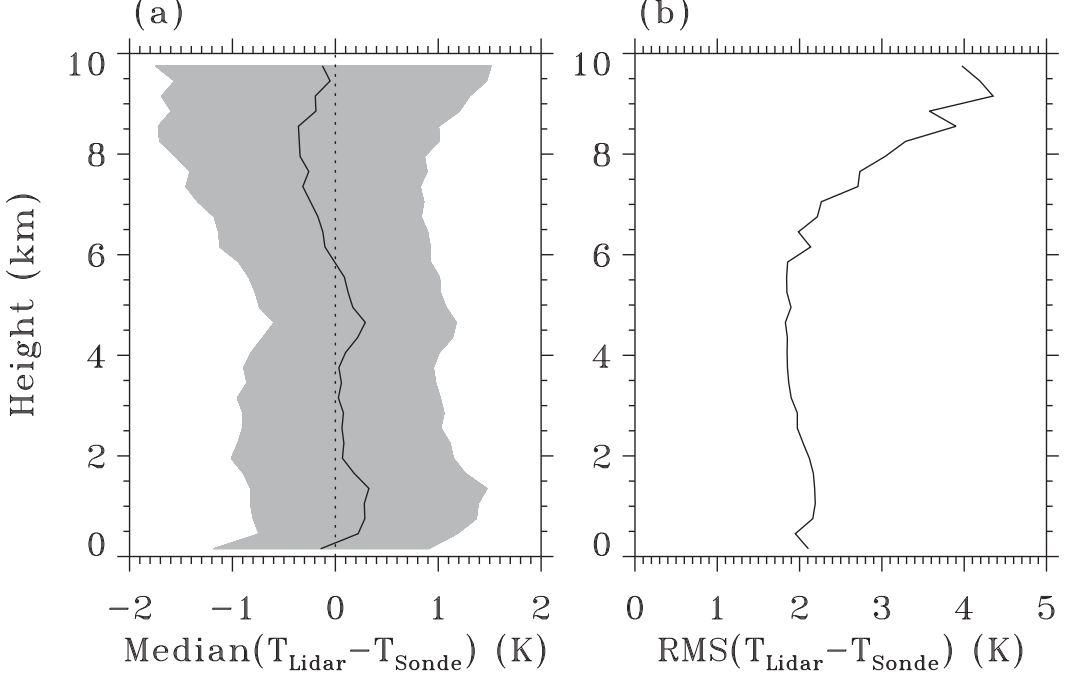


FIG. 17. Profiles of the (a) median and (b) RMS difference between the RL and radiosonde temperature for run type 2a using only noncalibration soundings. Statistics were derived from 1250 individual profiles acquired during clear-sky conditions between 1 Jan 2009 to 31 Dec 2010. The overall median difference is 0.005 K. The shaded region indicates the range of values between the 25th and 75th percentiles of the difference.

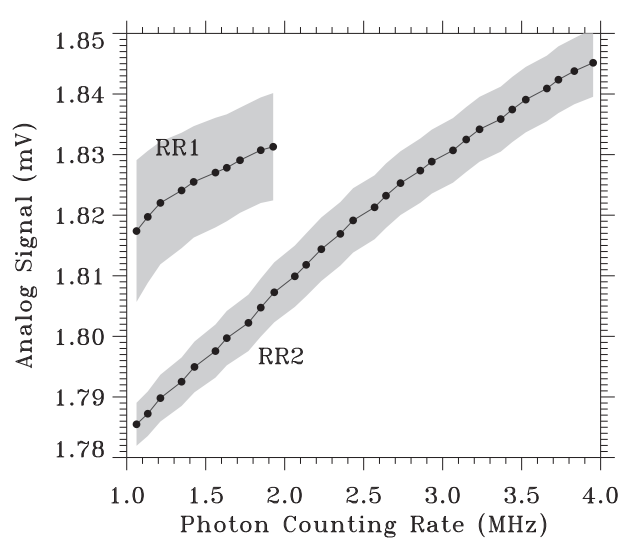


FIG. 18. Median analog voltage vs the photon counting rate (dead corrected) for the RR1 and RR2 detection channels. The curves were computed from a total of about 34 000 profiles (10-s time resolution) spanning 4 days of measurements (25, 26, 29, and 30 Jun 2012) and using only measurements within the calibration height range of 5 to 15 km AGL.

photon counting rate. Thus, as the solar background changes the linear response over the calibration band changes. This effect would in general cause the temperature calibration to change with changes in the solar background level.

5. Summary

The temperature profiling capability, accuracy, and calibration stability of the SGPRL were described. Temperature measurement is enabled through the use of two detection channels that sense Raman-shifted backscatter arising from rotational energy state transitions in atmospheric N2 and O2 molecules due to excitation at the laser wavelength of 355 nm. Interference filters are used to achieve narrowband detection. Raw signals from the detection channels are processed using an algorithm that was designed to run autonomously with very limited user intervention. The algorithm uses radiosonde data to perform calibration and overlap correction. The goal is to run the algorithm operationally within the ARM data management facility and to make the lidar temperature data available to the general science community through the ARM website (http://www.arm.gov/).

The accuracy and calibration stability of the SGPRL temperature measurements was assessed over a 2-yr period from 1 January 2009 to 31 December 2010. Results from run type 1 show that the calibration coefficients exhibit no significant long-term or seasonal

variation but do show a distinct diurnal variation. The ability to resolve this diurnal variability was made possible by the fact that radiosondes are launched once every 6 h at the SGP central facility. Results from run type 2, in which only nighttime radiosonde measurements were used for calibration, showed that the lidar exhibited a daytime warm bias that was correlated with the strength of the solar background signal. During the period near the summer solstice, the overall median bias reaches a maximum value of about 2.4 K at solar noon.

A scheme was developed to correct the calibration coefficients between sounding times and account for the diurnal bias. The motivation was to develop a calibration correction method that could be used in situations when radiosonde measurements are performed infrequently. The approach was to parameterize the calibration coefficients in terms of the solar background signal. The results showed that this scheme was effective at reducing the diurnal variation in the lidar temperature bias.

We believe that residual nonlinearities in the RR signals are the likely cause of the apparent correlation between the solar background and the temperature calibration. Our analysis indicates a slight nonlinearity in the response of the deadtime-corrected photon counting rate. This effect would likely cause small variations in the temperature calibration with changes in the solar background level.

Finally, we note that in December 2010, a second Raman lidar was deployed to the ARM facility in Darwin, Australia. This system is of nearly the same design as the SGPRL and thus contains the same temperature profiling capability. Efforts are currently under way to perform a similar long-term evaluation of the temperature measurements from that system.

Acknowledgments. We wish to thank the staff at the ARM SGP site and Chris Martin in particular for maintaining the operation of the Raman lidar. This research was supported by the Office of Biological and Environmental Research of the U.S. Department of Energy as part of the Atmospheric Radiation Measurement Climate Research Facility.

REFERENCES

Alexander, S. P., and T. Tsuda, 2008: High-resolution radio acoustic sounding system observations and analysis up to 20 km. J. Atmos. Oceanic Technol., 25, 1383–1396.

Alpers, M., R. Eixmann, C. Fricke-Begemann, M. Gerding, and J. Hoffner, 2004: Temperature lidar measurements from 1 to 105 km altitude using resonance, Rayleigh, and rotational Raman scattering. *Atmos. Chem. Phys.*, 4, 793–800.

- Arshinov, Y. F., S. Bobrovnikov, V. E. Zuev, and V. M. Mitev, 1983: Atmospheric temperature measurements using pure rotational Raman lidar. Appl. Opt., 22, 2984–2990.
- Balin, I., I. Serikov, S. Bobrovnikov, V. Simeonov, B. Calpini, Y. Arshinov, and H. V. D. Bergh, 2004: Simultaneous measurement of atmospheric temperature, humidity, and aerosol extinction and backscatter coefficients by a combined vibrational-pure-rotational Raman lidar. Appl. Phys., 79B, 775-782.
- Behrendt, A., and J. Reichardt, 2000: Atmospheric temperature profiling in the presence of clouds with a pure rotational Raman lidar by use of an interference-filter-based polychromator. *Appl. Opt.*, **39**, 1372–1378.
- —, T. Nakamura, M. Onishi, R. Baumgrat, and T. Tsuda, 2002: Combined Raman lidar for the measurement of atmospheric temperature, water vapor, particle extinction coefficient, and particle backscatter coefficient. Appl. Opt., 41, 7657–7666.
- —, —, and T. Tsuda, 2004: Combined temperature lidar for measurements in the troposphere, stratosphere, and mesosphere. Appl. Opt., 43, 2930–2939.
- Chandrasekhar Sarma, T. V., D. Narayana Rao, J. Furumoto, and T. Tsuda, 2008: Development of radio acoustic sounding system (RASS) with Gadanki MST radar—First results. *Ann. Geophys.*, **26**, 2531–2542.
- Cooney, J., 1972: Measurement of atmospheric temperature profiles by Raman backscatter. *J. Appl. Meteor.*, **11**, 108–112.
- Di Girolamo, P., R. Marchese, D. N. Whiteman, and B. Demoz, 2004: Rotational Raman lidar measurements of atmospheric temperature in the UV. *Geophys. Res. Lett.*, 31, L01106, doi:10.1029/2003GL018342.
- Feltz, W. F., W. L. Smith, H. B. Howell, R. O. Knuteson, H. Woolf, and H. E. Revercomb, 2003: Near-continuous profiling of temperature, moisture, and atmospheric stability using the atmospheric emitted radiance interferometer (AERI). J. Appl. Meteor., 42, 584–597.
- Ferrare, R. A., and Coauthors, 2006: Evaluation of daytime measurements of aerosols and water vapor made by an operational Raman lidar over the Southern Great Plains. *J. Geophys. Res.*, **111**, D05S08, doi:10.1029/2005JD005836.
- Goldsmith, J. E. M., F. H. Blair, S. E. Bisson, and D. D. Turner, 1998: Turn-key Raman lidar for profiling atmospheric water vapor, clouds and aerosols. *Appl. Opt.*, 37, 4979– 4990.
- Li, T., T. Leblanc, I. S. McDermid, P. Keckhut, A. Hauchecorne, and X. Dou, 2011: Middle atmosphere temperature trend and solar cycle revealed by long-term Rayleigh lidar observations. *J. Geophys. Res.*, **116**, D00P05, doi:10.1029/2010JD015275.

- Loehnert, U., D. D. Turner, and S. Crewell, 2009: Ground-based temperature and humidity profiling using spectral infrared and microwave observations. Part I: Simulated retrieval performance in clear-sky conditions. J. Appl. Meteor. Climatol., 48, 1017–1032.
- Luers, J. K., 1997: Temperature error of the Vaisala RS90 radiosonde. J. Atmos. Oceanic Technol., 14, 1520–1532.
- Mattis, I., D. Müller, A. Ansmann, U. Wandinger, J. Preißler, P. Seifert, and M. Tesche, 2008: Ten years of multiwavelength Raman lidar observations of free-tropospheric aerosol layers over central Europe: Geometrical properties and annual cycle. *J. Geophys. Res.*, 113, D20202, doi:10.1029/2007JD009636.
- Nedeljkovic, D., A. Hauchecorne, and M. Chanin, 1993: Rotational Raman lidar to measure the atmospheric temperature from the ground to 30 km. *IEEE Trans. Geosci. Remote Sens.*, 31, 90–101.
- Newsom, R. K., D. D. Turner, B. Mielke, M. F. Clayton, R. Ferrare, and C. Sivaraman, 2009: Simultaneous analog and photon counting detection for Raman lidar. *Appl. Opt.*, **48**, 3903–3914.
- Press, W. H., B. P. Flannery, S. A. Teukolsky, and W. T. Vetterling, 1988: Numerical Recipes in C. Cambridge University Press, 531 pp.
- Radlach, M., A. Behrendt, and V. Wulfmeyer, 2008: Scanning rotational Raman lidar at 355 nm for the measurement of tropospheric temperature fields. Atmos. Chem. Phys., 8, 159–169.
- Steinbrecht, W., H. Claude, F. Schönenborn, U. Leiterer, H. Dier, and E. Lanzinger, 2008: Pressure and temperature differences between Vaisala RS80 and RS92 radiosonde systems. J. Atmos. Oceanic Technol., 25, 909–927.
- Stokes, R. R., and S. E. Schwartz, 1994: The Atmospheric Radiation Measurement (ARM) program: Programmatic background and design of the cloud and radiation test bed. *Bull. Amer. Meteor. Soc.*, 75, 1201–1221.
- Turner, D. D., and J. E. M. Goldsmith, 1999: Twenty-four-hour Raman lidar water vapor measurements during the Atmospheric Radiation Measurement program's 1996 and 1997 water vapor intensive observation periods. J. Atmos. Oceanic Technol., 16, 1062–1076.
- ——, R. A. Ferrare, L. A. Heilman Brasseur, W. F. Feltz, and T. P. Tooman, 2002: Automated retrievals of water vapor and aerosol profiles from an operational Raman lidar. *J. Atmos. Oceanic Technol.*, 19, 37–50.
- Vaisala, cited 2010: Vaisala radiosonde RS92-D. Reference B210763EN-B, 2 pp. [Available online at http://www.vaisala. com/Vaisala Documents/Brochures and Datasheets/RS92-D-Datasheet-B210763EN-B-LoRes.pdf.]
- Whiteman, D. N., and Coauthors, 2006: Raman water vapor lidar measurements during the International H₂O Project. Part I: Instrumentation and analysis techniques. *J. Atmos. Oceanic Technol.*, 23, 157–169.